CRYSTAL GROWTH & DESIGN

Article

Cite This: Cryst. Growth Des. 2018, 18, 3244−3254

pubs.acs.org/crystal

Systematic Experimental and Computational Studies of Substituti and Hybridization Effects in Solid-State Halogen Bonded Assemblie

Suong T. Nguyen,[†,#] Thomas L. Ellington,[†,#] Katelyn E. Allen,[†,#] John D. Gorden,[‡] Arnold L. Rheingold,[§] Gregory S. Schumper,[†] Nathan H. Hammer,[†] and Davita L. Watkins[†]

[†]Department of Chemistry and Biochemistry, University of Mississippi, University, Mississippi 38677-1848, United States

[‡]Department of Chemistry and Biochemistry, Auburn University, Auburn, Alabama 36849-5312, United States

[§]Department of Chemistry, University of California, San Diego, La Jolla, California 92093-0358, United States

* Supporting Information

ABSTRACT: A quantitative assessment of the substituent, hybridization, and crystal-packing effects on the electronic, structural, and vibrational properties of halogen bonded systems is presented. Through a combined experimental and theoretical approach employing Raman spectroscopy, X-ray crystallography, and density functional theory, a series of solid-state iodobenzene and iodoethynylbenzene derivatives substituted with electron withdrawing -F, -(CF$_3$)$_2$, -F$_5$, and -(NO$_2$)$_2$) and their complexes with two pyridine-based building blocks are characterized. Structural analysis via X-ray crystallography and density functional theory computations suggests that these 1:1 molecular assemblies are not only driven by halogen bonding, but also by other energetically competitive noncovalent interactions, such as π-stacking. The magnitude of the σ-hole localized around the C−I bond in the isolated halogen bond (XB) donors and the interaction strength in the complexes unambiguously depend on the nature of the substituents on the donors and the hybridization of the carbon atom in the C−I bond. However, the vibrational C−I stretching frequency in the halogen bond donors and/or the change in that frequency accompanying XB formation are not solely controlled effects, but also by the coupling between the C−I stretch and other modes associated with the substituents on presence of various energetically competitive non-XB contacts in the solid cocrystals. In turn, this study highlig of conducting a comprehensive electronic and structural analysis of not only the halogen bond but also other in in the surrounding solid-state environment.

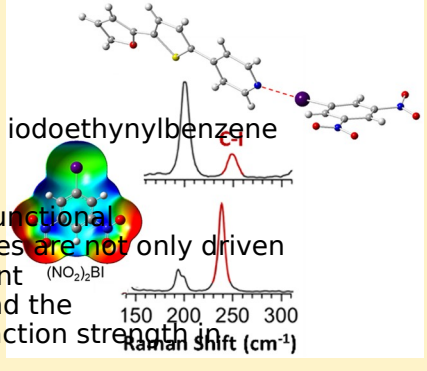

INTRODUCTION

Research in crystal engineering and materials science has revealed that noncovalent interactions play crucial roles in controlling the nanoscale architecture and also enhancing bulk properties.[1−6] Whereas hydrogen bonding has been extensively studied in the literature, the rising alternative-halogen bonding is less commonly discussed despite its applications in various chemical fields[7−12] such as medicinal chemistry[13−15] and organic synthesis.[16,17] A halogen bond (XB) is classified as a noncovalent interaction between an electrophilic region on a halogen atom (X) and a nucleophilic region on a Lewis base, typically in the form of a nitrogen, oxygen, or sulfur atom.[18] In this case, the halogen-containing molecule is referred to as the XB donor, while the Lewis base is the XB acceptor. The anisotropic redistribution of electron density as the C−X bond forms results in a localized region of positive electrostatic potential (ESP) that is aligned with the C−X covalent bond (i.e., the σ-hole) and a belt-like region of negative ESP that is found orthogonal to the C−X bond.[19−21] As such, the emergence of electropositive σ-hole affords nearly collinear intermolecular interactions that are thermodynamically stable, with interaction energies comparable to those of hydrogen bonding.[22,23] Although here the term "XB" concerns the intermolecular interaction of the σ-hole of a XB donor ar a XB acceptor (e.g., type-I XB), the occurrence of a second t of XB is also possible through the intermolecular interaction that σ-hole and the electronegative belt of XB donor (e.g., type-II XB).[24] The strength of a XB interaction depends on the electropositive region associated with the σ-hole and be tuned via modification of the halogen atom itself or the donor substituents. That is, as the halogen atom becomes more polarizable (I > Br > Cl ≫ F) and/or the XB donor substituents become more electron withdrawing, the σ-hole becomes more electropositive, typically resulting in stronger interactions.[21,23,25]

With increasing interest in this tunable noncovalent interaction, research has been focused on quantitative techniques used to accurately characterize XB interactions involving the σ-hole.[26−31] Among those, spectroscopic analyses—via infrared (IR), Raman, and nuclear magnetic resonance (NMR) spectroscopy—have been widely host

Received: March 14, 2018
Published: March 30, 2018

DOI: 10.1021/acs.cgd.8b00398
Cryst. Growth Des. 2018, 18, 3244−3254

adopted because they are sensitive enough to detect signatures of XB formation.[24,32−37] Studies employing these spectroscopic techniques typically correlate either vibrational (i.e., the C−X stretching modes) or chemical shifts associated with XB formation to the magnitude of the σ-hole and thus the strength of the interaction.[24,38−41] Although these procedures do serve as useful tools for describing and estimating the interaction strength of XBs, they are typically adopted when studying a systematic series of XB dimers that are not influenced by a complex environment, unlike those seen in XB cocrystals.[42] Fundamental analyses of XB driven assemblies suggest that the impact of additional factors, such as the environment surrounding a XB, can lead to more complicated behaviors.[15] Metrangolo and co-workers provided some early insight into this issue when they detected an unexpected high-frequency chemical shift upon XB formation from the solid-state ^{15}N NMR spectrum while attempting to evaluate the donor hierarchy, which they attributed to some unidentified non-XB interactions.[37] We have also observed similar anomalous behavior in a previous investigation into the electronic and spectroscopic properties of solution-phase XBs in the form of a downfield shift in the ^{13}C NMR spectrum of a XB complex between pyrimidine and pentafluorobenzene bromide, which was suggested to stem from secondary interactions imposed by the surrounding medium.[30] In a separate study, we showed that the presence of numerous energetically competitive non-XB intermolecular interactions in solid-state XB cocrystals resulted in complex crystal packing patterns and therefore affected the properties of XB interactions in those assemblies.[43]

Despite the number of unusual chemical shifts and/or vibrational complexation shifts associated with XB formation reported in the literature, to the best of our knowledge, there has not been any study that interrogates the influence of competitive non-XB intermolecular interactions on the vibrational properties of XBs that prompted us to probe not only the substituent and hybridization effects but also the impact of other concurrent non-XB contacts on the molecular properties of XB interactions in the solid state. Single-crystal X-ray structural analyses provided insights into the packing patterns of cocrystals as well as the geometrical parameters of all XB and non-XB interactions. Due to its low IR intensity in the fingerprint regions (100−500 cm^{-1}), the C−I stretching modes associated with XB interactions were detected via high resolution Raman spectroscopy.[40,44−46] Electronic structure theory computations were performed to explore the nature of the σ-hole on the iodine atom of a XB donor, aid in the assignment of the C−I stretching mode from the experimental Raman spectra, and determine the energetics of the pairwise contacts present in each cocrystal.

EXPERIMENTAL AND COMPUTATIONAL METHODS

Crystal Growth and X-ray Crystallography. Cocrystals were prepared in duplicate at a 1:1 XB acceptor/donor ratio by dissolving XB acceptor and donor in a chlorinated solvent (dichloromethane or chloroform) in a borosilicate glass vial. The resulting mixtures were ultrasonicated for 10 min. The open vial was placed in a secondary vial containing n-hexane or n-pentane. Using a vapor diffusion method, crystals were allowed to form at −5 °C over 3−7 days. Cocrystallization was confirmed through the comparison of melting points between the cocrystals and their corresponding monomers (i.e., both XB acceptors and donors if they exist in the solid state). A difference in the melting point of 14 °C between the cocrystals and the monomers was observed. Additional evidence of cocrystallization was also obtained using IR spectroscopy in combination with X-ray diffraction, the presence of XB interactions between the acceptors and donors was confirmed. A summary of the melting point and IR spectroscopic results can be found in the Supporting Information.

Geometries obtained from analyses are in good agreement with those reported in the literature.[36,41] Crystal investigation and data collection were conducted using a Bruker Kappa diffractometer with Mo Kα (λ = 0.71073 Å) radiation. Reflections were indexed by an automated indexing routine built in the APEXII program suite. The data analyses were carried out in Olex2 version 1.2,[48] using the program SHELXTL and in Discovery Studio Visualizer 2016. Crystal data and structure refinement parameters for all XB complexes are reported in the Supporting Information. The CCDC numbers for the single-crystal X-ray structures of each cocrystal are as follows: 1590272, 1590273, 1590264, 1590265, 1590274, 1590275, 1590276, 1502497, 1502498, 1502499, and 1502500.

Crystal Data for (NO$_2$)$_2$BI-PyrTF: $C_{19}H_{12}IN_3O_5S$ (M = 521.28 g/mol): monoclinic, space group $P2_1/c$ (No. 14), a = 12.157(2) Å, b = 11.475(2) Å, c = 14.470(3) Å, β = 108.05(3)°, V = 1919.1(7) Å^3, Z = 4, T = 100.0 K, μ(CuKα) = 14.470 mm^{-1}, D_{calc} = 1.804 g/cm^3, 11718 reflections measured (7.648° ≤ 2θ ≤ 136.346°), 3563 unique (R_{int} = 0.0418, R_{sigma} = 0.0357) which were used in all calculations. The final R_1 was 0.0285 (I > 2σ(I)) and wR_2 was 0.0731 (all data).

(NO$_2$)$_2$BI-PyrTF·$C_{19}H_{12}IN_3O_4S_2$ (M = 537.34 g/mol): monoclinic, space group $P2_1/n$ (No. 14), a = 5.826(2) Å, b = 7.991(2) Å, c = 41.935(8) Å, β = 91.01(3)°, V = 1952.0(9) Å^3, Z = 4, T = 100.0 K, μ(CuKα) = 15.182 mm^{-1}, D_{calc} = 1.828 g/cm^3, 10920 reflections measured (4.214° ≤ 2θ ≤ 136.356°), 3552 unique (R_{int} = 0.0547, R_{sigma} = 0.0589) which were used in all calculations. The final R_1 was 0.0562 (I > 2σ(I)) and wR_2 was 0.1385 (all data).

F_5BI-PyrTF·$C_{19}H_9F_5INOS$ (M = 521.25 g/mol): orthorhombic, space group $P2_12_12_1$ (No. 19), a = 5.8783(2) Å, b = 7.6445(2) Å, c = 39.6751(13) Å, V = 1782.87(10) Å^3, Z = 4, T = 180.45 K, μ(Mo Kα) = 1.973 mm^{-1}, D_{calc} = 1.9418 g/cm^3, 22280 reflections measured (4.1° ≤ 2θ ≤ 55.764°), 4248 unique (R_{int} = 0.0238, R_{sigma} = 0.0197) which were used in all calculations. The final R_1 was 0.0165 (I ≥ 2u(I)) and wR_2 was 0.0380 (all data).

F_5BI-PyrTF·$C_{19}H_9F_5INS_2$ (M = 537.32 g/mol): monoclinic, space group $P2_1$ (No. 4), a = 12.7948(4) Å, b = 5.8398(2) Å, c = 13.2832(4) Å, β = 109.251(1)°, V = 937.02(5) Å^3, Z = 2, T = 180.45 K, μ(Mo Kα) = 1.984 mm^{-1}, D_{calc} = 1.9043 g/cm^3, 23669 reflections measured (3.24° ≤ 2θ ≤ 54.214°), 4141 unique (R_{int} = 0.0358, R_{sigma} = 0.0296) which were used in all calculations. The final R_1 was 0.0210 (I ≥ 2u(I)) and wR_2 was 0.0469 (all data).

(NO$_2$)$_2$BAI-PyrTF.[43] $C_{21}H_{12}IN_3O_5S$ (M = 545.30 g/mol): monoclinic, space group $P2_1/n$ (No. 14), a = 19.084(4) Å, b = 30.968(6) Å, c = 14.021(3) Å, β = 94.66(3)°, V = 8259(3) Å^3, Z = 16, T = 100.0 K, μ(CuKα) = 13.485 mm^{-1}, D_{calc} = 1.754 g/cm^3, 70152 reflections measured (4.646° ≤ 2θ ≤ 136.488°), 14885 unique (R_{int} = 0.0697, R_{sigma} = 0.0511) which were used in all calculations. The final R_1 was 0.0486 (I > 2σ(I)) and wR_2 was 0.1176 (all data).

(NO$_2$)$_2$BAI-PyrTF.[43] $C_{21}H_{12}IN_3O_4S_2$ (M = 561.36 g/mol): triclinic, space group $P\bar{1}$ (No. 2), a = 8.3335(4) Å, b = 11.1648(6) Å, c = 12.4716(6) Å, α = 101.7030(10)°, β = 102.3030(10)°, γ = 107.2490(10)°, V = 1037.81(9) Å^3, Z = 2, T = 100.0 K, μ(MoKα) = 1.770 mm^{-1}, D_{calc} = 1.796 g/cm^3, 13674 reflections measured (3.086° ≤ 2θ ≤ 56.573°), 5133 unique (R_{int} = 0.0378, R_{sigma} = 0.0400) which were used in all calculations. The final R_1 was 0.0240 (I > 2σ(I)) and wR_2 was 0.0616 (all data).

F_2BAI-PyrTF.[43] $C_{21}H_{12}F_2INOS$ (M = 491.28 g/mol): monoclinic, space group $P2_1/n$ (No. 14), a = 10.681(2) Å, b = 4.221(2) Å, c = 40.107(8) Å, β = 92.85(3)°, V = 1805.7(10) Å^3, Z = 4, T = 100.0 K, μ(CuKα) = 15.293 mm^{-1}, D_{calc} = 1.807 g/cm^3, 12096 reflections measured (4.412° ≤ 2θ ≤ 137.398°), 3284 unique (R_{int} = 0.0399, R_{sigma} = 0.0309) which were used in all calculations. The final R_1 was 0.0296 (I > 2σ(I)) and wR_2 was 0.0766 (all data).

DOI: 10.1021/acs.cgd.8b00398
Cryst. Growth Des. 2018, 18, 3244−3254

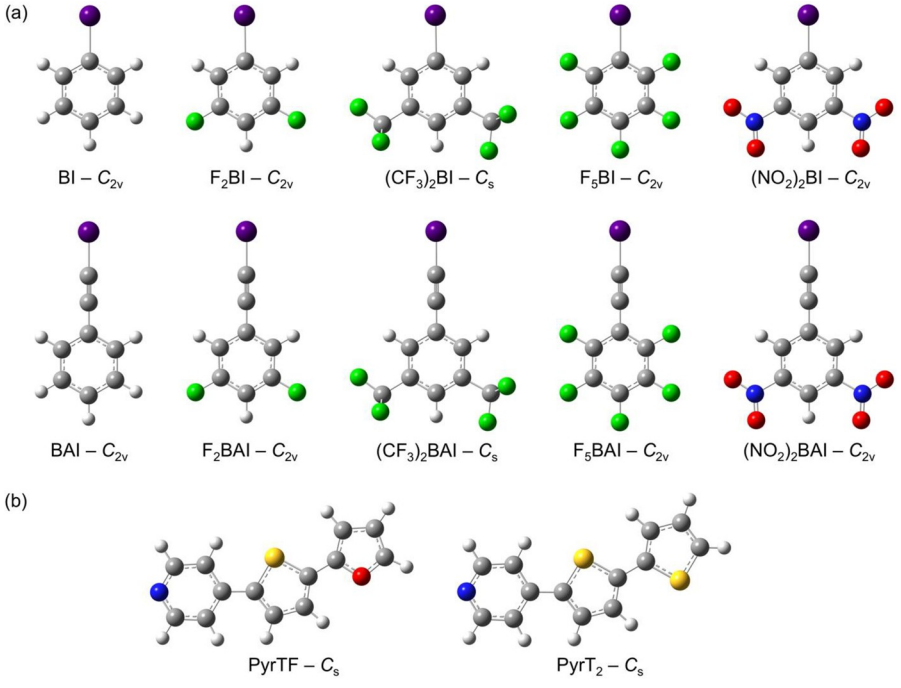

Figure 1. Molecular structures and point group symmetries of each XB (a) donor and (b) acceptor.

F_2BAI-PyrTF ($C_{21}H_{12}F_2INS_2$; M = 507.34 g/mol; triclinic, space group $P\bar{1}$ (No. 2), a = 4.0288(9) Å, b = 11.599(3) Å, c = 20.709(4) Å, α = 102.070(8)°, β = 92.784(7)°, γ = 93.486(9)°, V = 942.7(4) Å^3, Z = 2, T = 100.0 K, μ(MoKα) = 1.944 mm^{-1}, D_{calc} = 1.787 g/cm^3, 16735 reflections measured (3.6° ≤ 2θ ≤ 56.43°), 4633 unique (R_{int} = 0.0510, R_{sigma} = 0.0500) which were used in all calculations. The final R_1 was 0.0351 (I > 2σ(I)) and was wR_2 0.0799 (all data).

$(CF_3)_2$BAI-PyrTF ($C_{23}H_{12}F_6INOS$; M = 591.30 g/mol; triclinic, space group $P\bar{1}$ (No. 2), a = 9.0121(8) Å, b = 10.0224(8) Å, c = 24.324(2) Å, α = 81.838(3)°, β = 79.565(3)°, γ = 89.127(4)°, V = 2138.7(3) Å^3, Z = 4, T = 100.0 K, μ(MoKα) = 1.664 mm^{-1}, D_{calc} = 1.836 g/cm^3, 33610 reflections measured (4.106° ≤ 2θ ≤ 56.63°), 10344 unique (R_{int} = 0.0334, R_{sigma} = 0.0373) which were used in all calculations. The final R_1 was 0.0356 (I > 2σ(I)) and was wR_2 0.1053 (all data).

F_5BI-PyrTF ($C_{21}H_9F_5INOS$; M = 545.25 g/mol; triclinic, space group $P\bar{1}$ (No. 2), a = 8.3624(10) Å, b = 9.1257(11) Å, c = 12.6353(14) Å, α = 89.285(4)°, β = 80.621(4)°, γ = 88.933(4)°, V = 951.14(19) Å^3, Z = 2, T = 100 K, μ(MoKα) = 1.854 mm^{-1}, D_{calc} = 1.904 g/cm^3, 15770 reflections measured (4.938° ≤ 2θ ≤ 56.58°), 4670 unique (R_{int} = 0.0378, R_{sigma} = 0.0436) which were used in all calculations. The final R_1 was 0.0315 (I > 2σ(I)) and was wR_2 0.0721 (all data).

F_5BAI-PyrTF ($C_{21}H_9F_5INS_2$; M = 561.31 g/mol; triclinic, space group $P\bar{1}$ (No. 2), a = 5.0851(2) Å, b = 12.6790(6) Å, c = 15.6054(7) Å, α = 98.3090(10)°, β = 97.1630(10)°, γ = 99.8620(10)°, V = 969.28(7) Å^3, Z = 2, T = 100.0 K, μ(MoKα) = 1.923 mm^{-1}, D_{calc} = 1.923 g/cm^3, 11979 reflections measured (2.668° ≤ 2θ ≤ 50°), 3892 unique (R_{int} = 0.0279, R_{sigma} = 0.0227) which were used in all calculations. The final R_1 was 0.0164 (I > 2σ(I)) and was wR_2 0.0444 (all data).

Computational Methods. Full geometry optimizations and harmonic vibrational frequency computations with IR intensities and Raman activities were performed on the XB donors, acceptors, and the corresponding model complexes. The fully optimized geometries of the dimer complexes and corresponding fragments were used to compute binding energies ($E_{bind} = (E^{opt}_{complex} - E^{opt}_{donor} - E^{opt}_{acceptor})$, while the vibrational frequencies were used not only to verify whether each structure was a minimum (i.e., on the potential energy surface) but also to compare to the experimental Raman spectra. A full natural bond orbital (NBO)[49−56] analysis was performed to assess the magnitude of electron density transfer (|Δρ|) between each XB acceptor and donor pair in the XB model complexes. The maximum values of electrostatic potential corresponding to the σ-hole on the donor's iodine atom ($V_{s,max}$), which is commonly used to quantify the magnitude of the σ-hole,[24] were computed on the isolated XB donors. A set of single point energy computations with and without the Boys−Bernardi counterpoise (CP) procedure[57,58] was performed on the pairwise contacts found in the experimental XB crystal structures in order to determine their interaction energies ($E_{int} = E^{xtal}_{complex} - E^{xtal}_{donor} - E^{xtal}_{acceptor}$). The NBO analysis that was carried out on our model systems was extended to the pairwise contacts present in the experimental XB crystal structures.

All computations were performed using the Gaussian 09 software package and, where applicable, the analytic gradients and Hessians available therein.[59−61] The geometry optimizations, vibrational frequency computations, and NBO analyses used the global hybrid M06-2X[62] density functional in conjunction with a double-ζ correlation consistent basis set augmented with diffuse functions on all atoms (aug-cc-pVDZ) and a relativistic pseudopotential on iodine atoms (aug-cc-pVDZ for C, N, H, O, F, S and aug-cc-pVDZ-PP for I; denoted aVDZ).[59,60,63] All E_{bind} values are computed at the M06-2X/aVDZ level of theory. The set of single energy point computations employed the same M06-2X density functional with the analogous triple-ζ basis set and pseudopotential (aug-cc-pVTZ(-PP), denoted aVTZ).[59,60,63] As such, all reported E_{int} values are determined using the average of the necessary electronic energies (with and without CP corrections) from the M06-2X/aVTZ level of theory. These prescriptions were selected based on the extensive calibration by Kozuch and Martin.[64] The values of $V_{s,max}$ were determined using a critical point analysis within the Multiwfn package.[65] Additional details regarding these computations along with the optimized Cartesian coordinates and harmonic vibrational frequencies with Raman activities and IR intensities of each XB donor, acceptor, and their corresponding complexes can be found in the Supporting Information.

Raman Spectroscopy. A Horiba Scientific LabRAM HR Evolution Raman Spectroscopy system with charge coupled device (CCD) camera detection was used for the acquisition of solution and solid-phase Raman spectra. The confocal microscope and high throughput 800 mm single stage spectrometer of the LabRAM HR Evolution Raman spectrometer allowed for high-resolution imaging of the cocrystals as well as optimum spectral acquisition of all monomers

DOI: 10.1021/acs.cgd.8b00398
Cryst. Growth Des. 2018, 18, 3244−3254

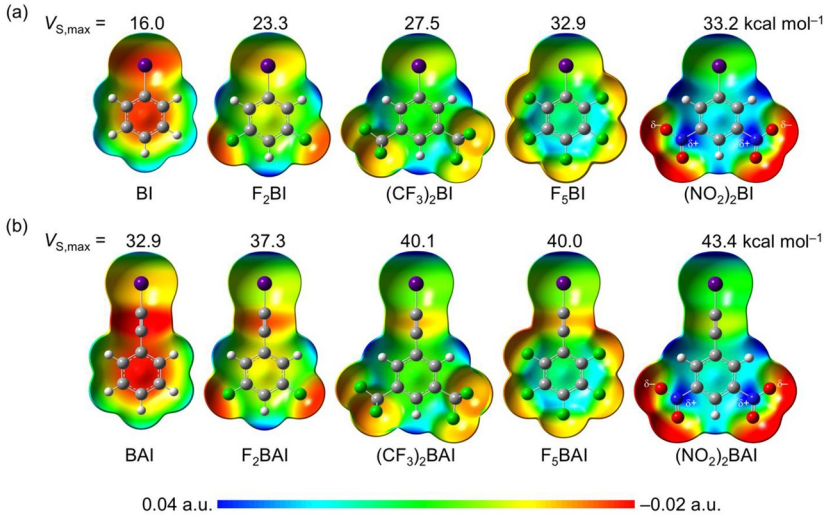

Figure 2. ESP maps and $V_{S,max}$ values of the (a) BI and (b) BAI XB donors using an electron isodensity of 0.0016 e bohr^{-3} at the M06-2X/aVDZ level of theory. $V_{S,max}$ values correspond to the magnitude of the σ-hole in kcal mol^{-1}.

and cocrystals. Spectra were obtained using a 785 nm diode laser and both 600 gr/mm and 1800 gr/mm diffraction gratings, allowing for accurate peak assignments with resolution of less than 1 cm^{-1}. The spectrum of each solid sample was optimized by locating a flat, semitransparent region of the sample with a high potential scattering utilizing the motorized stage and video features of the Raman spectrometer. For liquid samples, a macro-Raman accessory was utilized. To account for potential variations when comparing the solution-phase monomers to the solid-state cocrystals, temperature-controlled Raman spectra were acquired using a Linkam Scientific THMS600 microscope stage for all samples. The temperature-controlled Raman procedure used here is similar to the one recommended by Herrebout.[66]

RESULTS AND DISCUSSION

Design and Synthesis of XB Donors and Acceptors. Initially proposed for solid-state materials, the XB acceptors (Figure 1b), 4-(5-(furan-2-yl)thiophen-2-yl)-pyridine (PyrTF) and 4-([2,2′-bithiophen]-5-yl)pyridine (PyrT$_2$), were cocrystallized with iodobenzene and iodoethynylbenzene derivatives (XB donors; Figure 1a). PyrTF and PyrT$_2$ represent the derivatives of common organic semiconducting building blocks.[67−69] The pyridyl moiety is incorporated to guide the highly directional self-assembly of XB components. The planarity and rigidity of the backbone of conjugated thiophene and furan provide the framework for intermolecular overlap of π-orbitals in the solid-state, and an interplay of XB and π-stacking interactions that can be further utilized for crystal engineering and material applications.[70,71] Due to the high polarizability of iodobenzene derivatives are chosen as XB donors. The use of electron withdrawing substituents on the donor, possessing a strong inductive effect (e.g., $-(NO_2)_2$, and $-(CF_3)_2$), not only aids in the tuning of the interaction strength, but also affords 3D architectures due to their capacity to simultaneously participate in additional intermolecular contacts.[36,43,72] Furthermore, the hybridization of the carbon atom in the C−X bond of the XB donor influences the strength of the intermolecular interaction in which the higher s-character of the C_{sp}−X induces a repositioning of the electronegative belt on the halogen atom toward the triple bonded carbon C≡C atom (C_{sp}−X···π), and further increases the electropositive region on halogen atom.

Synthesis. The BI donors (i.e., BI, F_2BI, $(CF_3)_2$BI, F_5BI, and $(NO_2)_2$BI) were purchased from commercial sources and used without further purification. The synthesis of the XB acceptors (PyrTF and PyrT$_2$) and two BAI donors (F_5BAI and $(NO_2)_2$BAI) was reported in a previous work.[43] Additional detailed procedures to prepare BAI, F_2BAI, and $(CF_3)_2$BAI can be found in the Supporting Information. In general, Sonogashira coupling between substituted iodobenzene and trimethylsilylacetylene in the presence of catalytic amounts of tetrakis(triphenylphosphine)palladium and copper(I) iodide in toluene and diisopropylamine afforded the trimethylsilyl-(phenylethynyl)silane derivatives in good yield (69−71%). The trimethylsilyl group was then substituted with iodine by treating the compound with silver fluoride and N-iodosuccinimide in anhydrous acetonitrile in the absence of light. F_5BAI was afforded in 70% yield, while BAI and $(CF_3)_2$BAI were synthesized in 68% and 77% respectively, by using a modified procedure (see the Supporting Information).

Electronic Properties of XB Donors. In this study, we employed several computational techniques in order to accurately probe the electronic properties of the XB donors reported in Figure 1a, which provide the reference values needed for the characterization of XB complexes in subsequent sections. It should be noted that although the electrostatic potential (ESP) and the electron density are sometimes used interchangeably when discussing the magnitude of the σ-hole, the ESP at point r (V(r)) is not only a function of the electron density but also the atomic nuclei as seen in the first term of eq 1

$$V(r) = \sum_i \frac{Z_i}{|R_i - r|} - \int \frac{\rho(r')}{|r' - r|} dr' \quad (1)$$

where Z_i is the nuclear charge of atom i at position R_i, $\rho(r')$ is the molecular electron density. This and other misconceptions associated with halogen bonding and the models used to describe the interaction have been recently discussed in detail by Politzer, Murray and Clark.[73,74] In general, the magnitude of the σ-hole (i.e., the $V_{S,max}$ at the iodine atom) increases with the atomic number and the strength of the electron withdrawing substituents on the benzene moiety of the donors (-H < -F < $-(CF_3)_2$ < -F$_5$ < $-(NO_2)_2$) and as the hybridization of the

DOI: 10.1021/acs.cgd.8b00398
Cryst. Growth Des. 2018, 18, 3244−3254

carbon atom in the C−I bond is modified to sp^2 and so on. As can be seen in Figure 2a, the $V_{S,max}$ of the BI series ranges from 16.0 to 33.2 kcal mol^{-1}. The values tend to increase with (i) the electron withdrawing capability of the substituents (e.g., -$(CF_3)_2$ vs -F_2) and (ii) the number of those substituents present (e.g., -F_2 vs -F_5). More electropositive σ-holes are observed for the BAI series, where $V_{S,max}$ ranges from 32.9 to 43.4 kcal mol^{-1} (Figure 2b), but the trend remains the same. This enhancement of the σ-holes is due to the presence of acetylene linker, which increases the s-character of both C−I bonding and antibonding orbitals from roughly 17% for BI donors to 30% for BAI donors, as indicated by NBO analysis.

Structural Properties of XB Complexes. Cocrystals of the BI Series. A summary of the key geometrical parameters in both the computationally derived XB dimers and the experimental XB cocrystals between the BI donors and either acceptor is reported in Table 1. Precipitants were obtained

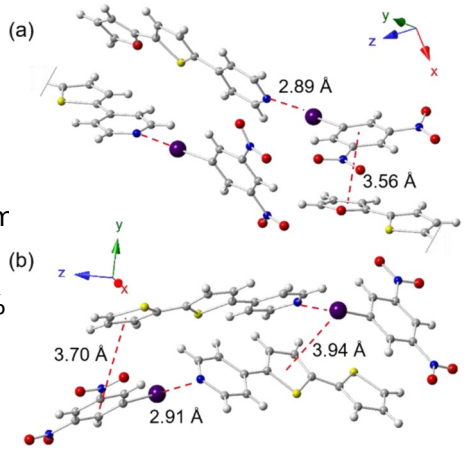

Figure 3. Packing diagram in (a) $(NO_2)_2$BI-PyrTF and (b) $(NO_2)_2$BI-$PyrT_2$, in which both XB and π-stacking are represented. Parts of the acceptor are removed for clarity purposes.

Table 1. XB Intermolecular Separations ($R_{I\cdots N}$, in Å), Angles ($\alpha_{C-I\cdots N}$, in °), and Percent Reduction in the Sum of van der Waals Radii (%rsvdW)[a] upon XB Formation for the M06-2X/aVDZ Model Dimers and the Corresponding Experimental Complexes Formed between the XB BI Donors and Acceptors

	theory			experiment		
complex	$R_{I\cdots N}$	$\alpha_{C-I\cdots N}$	%rsvdW	$R_{I\cdots N}$	$\alpha_{C-I\cdots N}$	%rsvdW
$(NO_2)_2$BI-PyrTF	2.92	180	30.0	2.89	169.0	30.7
$(NO_2)_2$BI-$PyrT_2$	2.92	180	30.0	2.91	175.4	30.2
F_5BI-PyrTF	2.86	180	31.4	2.89	174.9	30.7
F_5BI-$PyrT_2$	2.86	180	31.4	2.78	178.5	33.3

[a]Relative to the sum of nitrogen (1.79 Å) and iodine (2.38 Å) van der Waals radii.[75]

when cocrystallization was attempted for $(CF_3)_2$BI with either acceptor. That observation was substantiated by their model dimer's weak E_{bind}, low %rsvdW, and low $|\Delta\rho|$ values (Table S10) relative to those for the complexes reported in Table 1. In turn, cocrystals of $(NO_2)_2$BI and F_5BI with each acceptor were investigated. Despite using only a dimer to model the XB interaction in the crystal environment, there is good agreement between the theoretical and experimental data. The maximum and average absolute deviations (MAD and AAD) are 0.08 and 0.04 Å for $R_{I\cdots N}$, 11.0° and 5.6° for $\alpha_{C-I\cdots N}$, and 1.9 and 0.9 for %rsvdW, respectively. It should be noted that, although π-stacking plays the most competitive role in the observed crystal structures, contacts of that class in the BI cocrystals are severely limited in number due to the skewed orientation of the acceptors and donors in the XB interactions (Figures 3 and 4).

The 1:1 molecular assembly of $(NO_2)_2$BI-PyrTF exhibits a monoclinic structure with the $P2_1/n$ space group (Figure 3a). Its XB interaction connects the two monomers with an $\alpha_{C-I\cdots N}$ of 169.0° and $R_{I\cdots N}$ of 2.89 Å, corresponding to a %rsvdW of 30.7%. The average M06-2X/aVTZ computations with and without the CP procedure indicates that the interaction energy (E_{int}) of this pairwise contact in the cocrystal is −6.2 kcal mol^{-1} (Table S72). Various parallel-displaced π−π stacking interactions occur between (i) two thiophene moieties of acceptors (3.87 Å, E_{int} = −8.1 kcal mol^{-1}), (ii) the furan residue in PyrTF and the benzene ring in $(NO_2)_2$BI (3.56 Å, E_{int} = −7.4 kcal mol^{-1}), and (iii) the pyridine moiety of PyrTF and the benzene of $(NO_2)_2$BI (4.32 Å, E_{int} = −5.4 kcal mol^{-1})

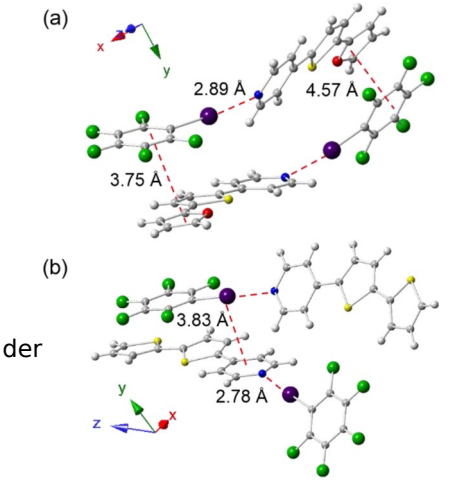

Figure 4. Packing diagram in (a) F_5BI-PyrTF and (b) F_5BI-$PyrT_2$.

(Table S72). Other secondary interactions involving the nitro groups were also observed (shown in greater detail in Figure S12 and Table S72).

The crystal structure of $(NO_2)_2$BI-$PyrT_2$ is very similar to that of $(NO_2)_2$BI-PyrTF as they have the same $P2_1/n$ space group (Figure 3b). In $(NO_2)_2$BI-$PyrT_2$, the $R_{I\cdots N}$ (2.91 Å) is slightly longer by 0.02 Å, the $\alpha_{C-I\cdots N}$ (175.4°) is closer to linearity by 6.4° (Table 1), and the XB interaction (E_{int} = −6.4 kcal mol^{-1}; Table S73) is slightly stronger by 0.2 kcal mol^{-1}. Here, the distribution of electron density of the donor and acceptor results in a face-to-face π-stacking interaction (3.7 Å, E_{int} = −8.8 kcal mol^{-1}; Figure S13-g and Table S73) between the thiophene in $PyrT_2$ and the benzene moiety in $(NO_2)_2$BI. Within the same contact, the iodine atom is positioned atop a central thiophene ring at a distance of 3.94 Å (Figure 3b). Similar to its PyrTF analogue, a variety of secondary interactions related to the nitro groups were detected in $(NO_2)_2$BI-$PyrT_2$ cocrystals, such as $O_{NO_2}\cdots N_{NO_2}$ (3.36 Å, E_{int} = −4.4 kcal mol^{-1}; Figure S13-b and Table S73).

Interchanging the donor from $(NO_2)_2$BI to F_5BI alters the structure and increases XB interaction strength by nearly 0.7 kcal mol^{-1} (in both PyrTF- and $PyrT_2$-complexes). Even though the $V_{S,max}$ value of the model F_5BI donor is approximately similar to that of $(NO_2)_2$BI (32.9 vs 33.2 kcal

DOI: 10.1021/acs.cgd.8b00398
Cryst. Growth Des. 2018, 18, 3244−3254

Table 2. XB Intermolecular Separations ($R_{I\cdots N}$ in Å), Angles ($\alpha_{C-I\cdots N}$ in °), and Percent Reduction in the Sum of van der Waals Radii (%rsvdW)[6] upon XB Formation for the M06-2X/aVDZ Model Dimers and the Corresponding Experimental Comp Formed between the XB BAI Donors and Acceptors

	theory			experiment		
complex	$R_{I\cdots N}$	$\alpha_{C-I\cdots N}$	%rsvdW	$R_{I\cdots N}$	$\alpha_{C-I\cdots N}$	%rsvdW[6]
$(NO_2)_2$BAI-PyrTF[b]	2.82	180	32.4	2.67−2.76	174.9	33.8−36.0
$(NO_2)_2$BAI-PyrT$_2$	2.82	180	32.4	2.70	174.5	35.3
F_2BAI-PyrTF	2.86	180	31.4	2.78	178.7	33.3
F_2BAI-PyrT$_2$	2.86	180	31.4	2.76	178.1	33.8
$(CF_3)_2$BAI-PyrTF	2.84	180	31.9	2.75	177.4	34.1
$(CF_3)_2$BAI-PyrT$_2$[a]	2.84	180	31.9			
F_5BAI-PyrTF	2.83	180	32.1	2.71	179.0	35.0
F_5BAI-PyrT$_2$	2.83	180	32.1	2.71	178.0	35.0
MAD				0.15	5.5	3.6
AAD				0.11	2.8	2.5

[a]X-ray single crystal structure was not obtainable due to fragility of crystals. [b]Multiple XB interactions were observed in the experimental cocrystal.[43] [c]Relative to the sum of nitrogen (1.79 Å) and iodine (2.38 Å) van der Waals radii.[35] [d]Values previously reported.[43]

mol^{-1}). In the case of F_5BI-PyrTF, XB dimers pack in an orthorhombic pattern of the $P2_12_12_1$ space group (Figure 4a), in which $\alpha_{C-I\cdots N}$ is 174.9°, $R_{I\cdots N}$ is 2.89 Å corresponding to a %rsvdW of 30.7% (Table 1), and the computed E_{int} is −6.9 kcal mol^{-1} (Table S74). The presence of five F substituents contributes to the observation of two distinctive π-stacking interactions between the pentafluorobenzene ring of F_5BI and one of the moieties of PyrTF at the distances of 3.75 Å (E_{int} = −5.8 kcal mol^{-1}) and 4.57 Å (E_{int} = −5.9 kcal mol^{-1}) (Figure 4a, Figure S14-a,b, and Table S74).

A decrease in $R_{I\cdots N}$ (0.11 Å) and increase in linearity of $\alpha_{C-I\cdots N}$ (3.6°) were observed when PyrT$_2$ was used in place of PyrTF as the acceptor for cocrystallization. The monoclinic assembly of F_5BI-PyrT$_2$ whose space group is $P2_1$ (Figure 4b), $R_{I\cdots N}$ (2.78 Å) is the shortest XB distance and its $\alpha_{C-I\cdots N}$ (178.5°) is the closest to linearity when compared to that of the BI complexes (Table 1). Moreover, that XB interaction is the strongest (E_{int} = −7.2 kcal mol^{-1}) among the BI cocrystals considered here (Table S75). The π-stacking interaction between the thiophene moiety of the acceptor and the benzene ring of the donor exhibits an intermolecular distance of 3.63 Å (Figure 4b) and a computed E_{int} of −8.1 kcal mol^{-1} (Table S75). This relatively strong dispersion interaction involves the π-cloud of the pyridine moiety and the electronegative belt of the iodine atom (Figure S15-d).

Cocrystals of the BAI Series. We now move our attention to the structural characteristics of the XB BAI complexes. The key geometrical parameters for the BAI series of XB contact model dimers and experimental cocrystals are reported 2. The single crystal structure of $(CF_3)_2$BAI-PyrT$_2$ could not be obtained due to the fragility of crystals. In general, the XB interaction strengths are on the same order of magn those found in the BI cocrystals. With the exception of $(NO_2)_2$BAI-PyrTF,[43] the packing patterns observed in the B complexes exhibit a near coplanar arrangement. This affords denser cocrystals with tighter stacking configurations. Although the agreement between the theoretically predicted and the experimentally determined key geometrical parameters is slightly less than in the BI series, they still fall within the error associated with the level of theory employed here.

The structural analysis for XB complexes comprised of $(NO_2)_2$BAI and F_2BAI donors with both PyrTF and PyrT$_2$ acceptors was reported in our previous study.[43] Cocrystals containing $(NO_2)_2$BAI exhibit competing noncovalent interactions, where π-stacking between pairs of donor molecules and donor−acceptor monomers were ~2 kcal mol^{-1} stronger than XBs. Exhibiting a monoclinic structure with a $P2_1/c$ space group, $(NO_2)_2$BAI-PyrTF crystal structure displays high levels of disordering which are evident by the presence of four dist XB interactions. By contrast, $(NO_2)_2$BAI-PyrT$_2$ gives rise to a more ordered solid-state assembly exhibiting a triclinic structure with a $P\bar{1}$ space group. XB is characterized by an $\alpha_{C-I\cdots N}$ of 174.5° and a $R_{I\cdots N}$ of 2.70 Å with an E_{int} of −8.7 kcal mol^{-1}. The variations between these two cocrystals are due to the nitro groups on the XB donor participating in various secondary interactions that act in both stabilizing (i.e., $(NO_2)_2$BAI-PyrT$_2$ and destabilizing ($(NO_2)_2$BAI-PyrTF manners.[43] Cocrystals containing F_2BAI consist of associative XB monomers that participate in nearly cofacial π−π interactions. F_2BAI-PyrTF ($\alpha_{C-I\cdots N}$ of 178.7°, $R_{I\cdots N}$ of 2.78 Å, E_{int} of −7.5 kcal mol^{-1}) exhibits a monoclinic structure with the $P2_1/c$ space group where F···H interactions contribute to the isotropic packing behavior of the F_2BAI-PyrT$_2$ yields crystallization in the triclinic space group $P\bar{1}$. XB is characterized by an $\alpha_{C-I\cdots N}$ of 178.1° and a $R_{I\cdots N}$ of 2.76 Å with an E_{int} of −7.6 kcal mol^{-1}.[43]

The 1:1 assembly of $(CF_3)_2$BAI-PyrTF exhibits a nearly coplanar parallel packing pattern of the triclinic space group $P\bar{1}$ (Figure 5). The two associative monomers form a XB contact

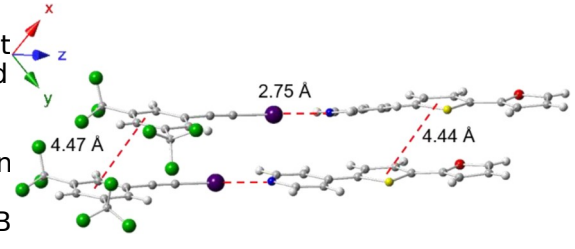

Figure 5. Packing diagram in $(CF_3)_2$BAI-PyrTF.

with an $\alpha_{C-I\cdots N}$ of 177.4°, a $R_{I\cdots N}$ of 2.75 Å, corresponding to a %rsvdW of 34.1%, and an E_{int} of −7.9 kcal mol^{-1} (Table S76). The acidic proton attached to the ortho-carbon on the furan moiety promotes adjacent rows of XB complexes via its interaction with the π-orbitals of the acetylene linker of the donor (3.01 Å, E_{int} = −0.8 kcal mol^{-1}; Figure S16-c and Table S76). Other intermolecular contacts also contribute to the

DOI: 10.1021/acs.cgd.8b00398
Cryst. Growth Des. 2018, 18, 3244−3254

packing pattern of the assembly, such as $H_{thiophene}\cdots F$ (2.54 Å, E_{int} = −1.3 kcal mol^{-1}; Figure S16-d and Table S76). In addition, more energetically competitive parallel-displaced π-stacking contacts between the two PyrTF acceptors (4.44 Å, E_{int} = −8.3 kcal mol^{-1}) and between the donors (4.47 Å, −5.0 kcal mol^{-1}) are also observed in the cocrystal (Figure S16-a,b and Table S76).

Similar to that of $(CF_3)_2$BAI-PyrTF, the 1:1 assembly of F_5BAI-PyrTF exhibits $P\bar{1}$ space group symmetry, in which each XB dimer is antiparallel to each other (Figure 6a). This

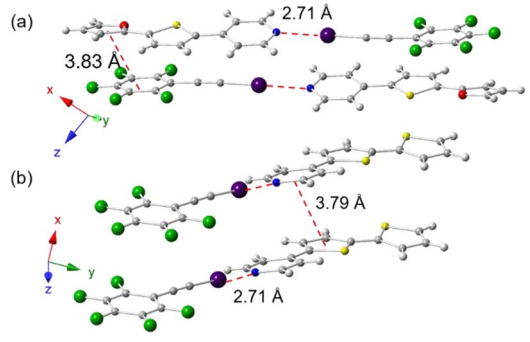

Figure 6. Packing diagram in (a) F_5BAI-PyrTF and (b) F_5BAI-$PyrT_2$.

arrangement is in part supported by other favorable interactions such as ortho-$H\cdot\pi_{C\tau C}$ (2.82 Å, E_{int} = −2.1 kcal mol^{-1}) and $H_{thiophene}\cdots F$ (2.39 Å, E_{int} = −1.4 kcal mol^{-1}) (Figure S17-c,e and Table S77). XB interactions within this cocrystal are characterized by a distance of 2.71 Å associated with a $I\cdots N$ %rsvdW, a nearly linear $C-I\cdots N$ of 179°, and an E_{int} of −8.1 kcal mol^{-1}. Competing with the XB contact is the strong parallel-displaced π-stacking between the furan moiety of the acceptor and pentafluorobenzene ring of the donor (3.83 Å, E_{int} = −8.8 kcal mol^{-1}; Figure S17-a and Table S77).

F_5BAI-$PyrT_2$ exhibits a comparable antiparallel packing pattern of the space group $P\bar{1}$ (Figure 6b), in which the donor and the acceptor associate via a XB contact whose %rsvdW, $C-I\cdots N$, and E_{int} are 2.71 Å, 85.0%, 178°, and −8.0 kcal mol^{-1}, respectively. The crystal packing of F_5BAI-$PyrT_2$ is also supported by numerous non-XB pairwise contacts, $H_{thiophene}\cdots\pi(C\tau C)$ (2.91 Å, E_{int} = −1.6 kcal mol^{-1}) and $H_{thiophene}\cdots F$ (2.33 Å, E_{int} = −1.2 kcal mol^{-1}) (Figure S18-d,e and Table S78). Multiple π-stacking interactions (E_{int} from −5.2 to −6.5 kcal mol^{-1}) are present but weaker than XB contact (Figure S18-a,b,f and Table S78).

Spectroscopic Analysis of XB Donors and Their Corresponding XB Cocrystals. Vibrational shifts in various stretching modes, particularly those with distinctive spectroscopic signatures (C−H, C−X, C−Y where Y = N, O, S), have been commonly used to detect formation of XB interactions.[24,36,41,76,77] Although the CτC stretch has also been used elsewhere in this context, it is very sensitive to non-XB contacts and can lead to unsystematic behavior of vibrational frequency shifts in turn.[30] and others[25,26,31,35,38,40,41,45,46,66,78] have taken an alternative approach involving the interrogation of the C−I stretching mode and their shifts upon XB formation as they are far more sensitive to halogen bond formation.[79]

XB Donors. For the BI series, the computed and experimental C−I stretching frequencies correlate well with each other with a MAD of 7 cm^{-1} (F_5BI) and an AAD of 4 cm^{-1} (Table S67). This agreement facilitates the assignment of C−I stretching modes in the experimental spectra of BI donors. The same comparison for the BAI series reveals an agreement between theory and experiment for BAI and F_5BAI (3 cm^{-1} in both cases); however, deviations occur for $(CF_3)_2$BAI (13 cm^{-1}) and $(NO_2)_2$BAI (17 cm^{-1}) (Table S69). The experimental Raman spectra shown in the first column of Figure 7a,b show a dependence of the C−I stretching frequency on the properties of donor substituents as well as the hybridization of the carbon atom in the C−I bond. That is, as the hybridization of the carbon atom of the C−I bond is modified from sp^2 to sp, the frequency of the C−I stretch undergoes a "red shift" (i.e., shift to lower energy). The presence of electron withdrawing groups also leads to red

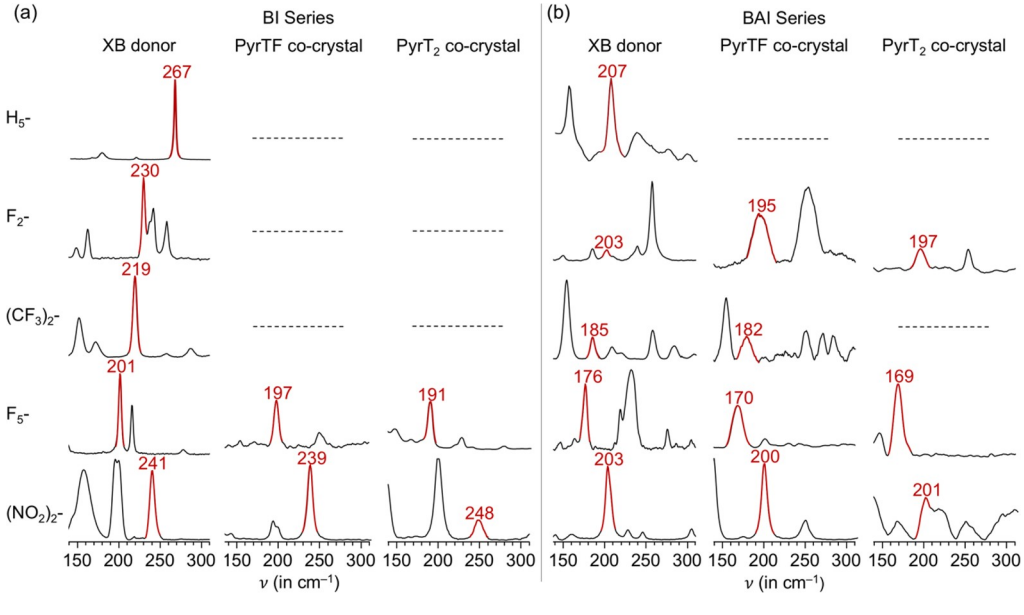

Figure 7. Experimental Raman spectra of the region associated with the C−I stretching mode (red peaks with values directly a series and (b) the BAI series of XB donors and their cocrystals with the acceptors PyrTF and $PyrT_2$

DOI: 10.1021/acs.cgd.8b00398
Cryst Growth Des 2018, 18, 3244−3254

shifting in the C−I stretching frequency when compared to the unsubstituted donors (i.e., BI and/or BAI). However, an inconsistent trend (i.e., does not directly correlate with electron withdrawing ability) in the C−I stretching frequency (ν_{C-I}) shifts ($-NO_2 > -F > -(CF_3)_2 > -F_5$) was observed for both BI and BAI series of XB donors. Herein, this irregular behavior is attributed to the vibrational coupling between the C−I stretch and other vibrational modes, such as the in-plane symmetric rocking of $-CF_3$ and $-NO_2$ groups. To test this hypothesis, vibrational frequencies in a series of para-monosubstituted XB donors (i.e., CF_3BI, and NO_2BI), were computed (Table S70). The results indicate that when such vibrations are not coupled, as is the case of this para-monosubstituted series, the ordering of the C−I stretching frequencies does indeed correlate with the electron withdrawing ability of the substituents and of the V$_{S,max}$ of the XB donors: BI < FBI < CF_3BI < NO_2BI (see the Supporing Information for full detail).

BI Cocrystals. The Raman spectra for the BI cocrystals are reported in Figure 7a. The computed C−I stretching frequencies for the BI series of dimers agree well with their experimental counterparts (MAD = 8 cm^{-1}, AAD = 5 cm^{-1}; Table S68). In addition, their ordering is consistent with theory; however, it should be noted that only four of the BI series cocrystals were obtained (BI-PyR and $(NO_2)_2$BI-PyR, where R is either -TF$_2$ or -T$_2$). In addition to the shifts in the C−I stretching frequency arising from substituent and hybridization effects, this frequency is further red-shifted upon XB formation (i.e., complexation shifts). These complexation shifts are commonly rationalized by either charge transfer or the net electrostatic attraction between the nonbonding electrons of the nitrogen atom and the electropositive σ-hole of iodine atom.[24,31,78] Both processes tend to weaken the C−I bond through the enhancement of its antibonding character and in turn, lead to the observed perturbation of its vibrational stretching frequency.

As seen in the second and third columns of Figure 7a, the C−I stretching frequency shifts of the complexes with either acceptor is lower than that of $(NO_2)_2$BI. Through comparing the C−I stretching frequencies of the XB donors and the XB complexes, a red shift is observed for BI-PyrTF (−4 cm^{-1}) and F$_5$BI-PyrT$_2$ (−11 cm^{-1}). At first glance, these results suggest that the C−I stretching vibration does depend on the identity of the acceptor. However, armed with the knowledge regarding the surrounding environment, it becomes clear that the variations between the complexation shifts of F$_5$BI-PyrTF and F$_5$BI-PyrT$_2$ are due to the dominant non-XB contacts found in the cocrystals described earlier in this work. This abnormal behavior extends to $(NO_2)_2$BI-PyrTF and $(NO_2)_2$BI-PyrT$_2$ as they show somewhat large variations between the magnitude of their complexation shifts. In the case of $(NO_2)_2$BI-PyrT$_2$, the C−I stretching frequency actually undergoes a "blue shift" (i.e., higher energy) of +7 cm^{-1}. The complexation shifts computed between the isolated $(NO_2)_2$BI and the corresponding cocrystals are dissimilar to those computed for the other cocrystals studied in this work. More specifically, the nitro containing XB donors are the only ones that naturally exist in the solid-state and thus require the surrounding environment of the $(NO_2)_2$BI single crystal be taken into consideration. The computation of the corresponding complexation shifts likewise. Of the other cocrystals considered, the C−I stretching frequency of the XB donor in this particular case, however, an intermolecular XB interaction in the isolated $(NO_2)_2$BI crystal is detected between the iodine atom of XB donor and the oxygen atom of another XB donor (i.e., an I···O XB interaction).[80] This observation, in addition to the same vibrational coupling of $-NO_2$ detected in the $(NO_2)_2$BI XB donor leads to the anomalous behavior seen in the C−I stretching frequency of $(NO_2)_2$BI-PyrTF and $(NO_2)_2$BI-PyrT$_2$ cocrystals.

BAI Cocrystals. The Raman spectra for the BAI cocrystals are reported in Figure S71. Similar to the XB donors and the BI cocrystals, the theoretical and experimental C−I stretching frequencies of the BAI cocrystals agree well, having a MAD and AAD of 12 and 6 cm^{-1}, respectively (Table S69). Additionally, their theoretical and experimental trends with either acceptor are consistent, but their unexpected blue shifts (F$_5$BAI-PyrTF < $(CF_3)_2$BAI-PyrTF < F$_2$BAI-PyrTF < $(NO_2)_2$BAI-PyrTF and F$_5$BAI-PyrT$_2$ < F$_2$BAI-PyrT$_2$ < $(NO_2)_2$BAI-PyrT$_2$. It should be pointed out that the variations between BAI cocrystals comprised of PyrTF and/or PyrT$_2$ are smaller (±2 cm^{-1}) than those containing XB donors (−6 and +9 cm^{-1} for PyrTF and PyrT$_2$ cocrystals, respectively). This suggests that in these BAI cocrystals, competitive interactions have far less pronounced effect on the C−I vibrational signatures.

The vibrational shifts that accompany XB formation in the BAI series of cocrystals, however, are seemingly "random" ($(NO_2)_2$BAI-PyrTF < $(CF_3)_2$BAI-PyrTF < FBAI-PyrTF < F$_2$BAI-PyrTF and $(NO_2)_2$BAI-PyrT$_2$ < F$_2$BAI-PyrT$_2$ < F$_5$BAI-PyrT$_2$) and do not reflect the order of electron withdrawing ability of the substituents. As discussed above, this unusual trend and performance is in part a consequence of the vibrational coupling between the C−I stretching and other vibrational modes. Moreover, the presence of a I···O XB contact in the isolated $(NO_2)_2$BAI (this work; CCDC: 1524553) donor crystal, most likely plays a role in the observed trend. Finally, as conveyed in the structural analysis of the cocrystals, the XB donors in F$_2$BAI-PyrTF, F$_2$BAI-PyrT$_2$, and $(CF_3)_2$BAI-PyrTF each form homogeneous donor−donor interactions in the form of π-stacking (E_{int} = −3.7, −4.5, and −5.0 kcal mol^{-1}, respectively). In those $\pi_{donor}\cdots\pi_{donor}$ contacts, the C−I bond is roughly parallel and stacked on top of the C≡C bond, much like that of type-II halogen bonds.[22,24] This results from a NBO analysis suggests that the π-orbitals around the C≡C region could perturb the electron density on the C−I bond and in turn contribute to the unpredicted trend in the vibrational C−I stretching shifts in these complexes.

CONCLUSION

In summary, we investigate the substituent, hybridization, and crystal packing effects on the electronic, structural, and spectroscopic properties of two series of XB donors and the 1:1 molecular assemblies formed between them and one of two XB acceptors.

Substituents on the XB donors and the hybridization of the carbon atom in the C−I bond substantially impact the electronic and structural properties of the cocrystals (e.g., magnitude of the σ-hole, the intermolecular I and N distances, and the interaction strength of XB contacts). Moreover, strong electron withdrawing substituents (e.g., $-NO_2$ and -F$_5$) also promote intermolecular π-stacking interactions between the acceptors and donors that are energetically stronger than the corresponding XB contacts by 0.7−2.4 kcal mol^{-1}. Additionally, the presence of the triple bond in the BAI donors alters the geometries of XB interactions, resulting in near coplanar XB contacts, thus stimulating a greater number of competing pairwise non-XB contacts than those found in the BI series.

DOI: 10.1021/acs.cgd.8b00398
Cryst. Growth Des. 2018, 18, 3244−3254

Although the identity of substituents and the hybridization of the carbon atom in the C$_{\tau}$C bond undoubtedly influence the vibrational stretching frequency of the C−I bond within XB complexes, they do not solely govern the vibrational complexation shifts that accompany XB formation. Information on vibrational coupling between the C−I stretching and other modes within the XB donor and the presence of numerous energetically competitive intermolecular interactions among the donors and acceptors that considerably and unpredictably alter the vibrational signatures of the corresponding XB cocrystals. The electronic, structural, and vibrational analysis presented here suggest that the characterization of XBs not only relies on the molecular properties of the monomeric XB donor (or and/or acceptor) but also on the chemical environment surrounding those XB interactions. As such, it is recommended that a holistic approach, employing a diverse set of quantitative techniques, should be adopted when attempting to accurately characterize such interactions in the solid state.

ASSOCIATED CONTENT

Supporting Information

The Supporting Information is available free of charge on the ACS Publications website at DOI: 10.1021/acs.cgd.8b00398.

Experimental details regarding crystallographic data, details on thermal analysis, theoretical calculations, ^{1}H NMR spectra and supplementary results (PDF)

Accession Codes

CCDC 1502497−1502500, 1590264−1590266, and 1590272−1590276 contain the supplementary crystallographic data for this paper. These data can be obtained free of charge via www.ccdc.cam.ac.uk/data_request/cif, or by emailing data_request@ccdc.cam.ac.uk, or by contacting The Cambridge Crystallographic Data Centre, 12 Union Road, Cambridge CB2 1EZ, UK; fax: +44 1223 336033.

AUTHOR INFORMATION

Corresponding Authors

*(G.S.T.) E-mail: tschumpr@olemiss.edu.
*(N.I.H.) E-mail: nhammer@olemiss.edu.
*(D.L.W.) E-mail: dwatkins@olemiss.edu.

ORCID

Suong T. Nguyen: 0000-0002-5745-9096
Gregory T. Tschumper: 0000-0002-3933-2200
Nathan I. Hammer: 0000-0002-6221-2709
Davita L. Watkins: 0000-0002-0943-7220

Author Contributions

#S.T.N., T.L.E., and K.E.A. all contributed equally to this work.

Author Contributions

All authors have given approval to the final version of the manuscript.

Notes

The authors declare no competing financial interest.

ACKNOWLEDGMENTS

S.T.N and D.L.W. appreciate financial support of this work from the National Science Foundation CAREER Award under Grant Numbers CHE-1652094. N.I.H. and K.E.A. thank the National Science Foundation for supporting this work through Grant OIA-1539035. The computational work is supported by the Mississippi Center for Supercomputing Research and the National Science Foundation under Grant Numbers OIA-1430364 and CHE-1664998 (T.L.E. and G.S.T.).

REFERENCES

(1) Jheng, J.-F.; Lai, Y.-Y.; Wu, J.-S.; Chao, Y.-H.; Wang, C.-L.; Hsu, C.-S. Influences of the Non-Covalent Interaction Strength on Reaching High Solid-State Order and Device Performance of Bandgap Polymer with Axisymmetric Structural Units. Adv. Mater. 2013, 25, 2445−2451.

(2) Wang, D.; Tong, G.; Dong, R.; Zhou, Y.; Shen, J.; Zhu, X. Self-assembly of supramolecularly engineered polymers and their biomedical applications. Chem. Commun. 2014, 50, 11994−12017.

(3) Nguyen, T. L.; Choi, H.; Ko, S. J.; Uddin, M. A.; Walker, B.; Yum, S.; Jeong, J. E.; Yun, M. H.; Shin, T. J.; Hwang, S.; Kim, J. Y.; Woo, H. Y. Semi-crystalline photovoltaic polymers with efficiency exceeding 9% in a [similar]300 nm thick conventional single-cell device. Energy Environ. Sci. 2014, 7, 3040−3051.

(4) Ebring, B.; Romero, B.; Serrano, J. L.; Folcia, C. L.; Etxebarria, J.; Ortega, J.; Termine, R.; Golemme, A.; Giménez, R.; Sierra, T. H-Bonded Donor−Acceptor Units Segregated in Coaxial Columnar Assemblies: Toward High Mobility Ambipolar Organic Semiconductors. J. Am. Chem. Soc. 2016, 138, 12511−12518.

(5) Fang, R.; Chen, R.; Gao, J.; Zhang, H.; Wu, H.; Li, H. Chalcogen bridged pyrene derivatives: synthesis, crystal−packing structures and field effect transistors properties. Org. Electron. 2017, 45, 108−114.

(6) Liu, H.; Huang, L.; Cheng, X.; Hu, A.; Xu, H.; Chen, L.; Chen, Y. N-type Self-Doping of Fluorinated Conjugated Polyelectrolytes for Polymer Solar Cells: Modulation of Dipole, Morphology, and Conductivity. ACS Appl. Mater. Interfaces 2017, 9, 1145−1153.

(7) Meyer, F.; Dubois, P. Halogen bonding at work: recent applications in synthetic chemistry and materials. CrystEngComm 2013, 15, 3058−3071.

(8) Zhu, W.; Zheng, R.; Zhen, Y.; Yu, Z.; Dong, H.; Fu, H.; Shi, Q.; Hu, W. Rational Design of Charge-Transfer Interactions in Halogen-Bonded Co-crystals toward Versatile Solid-State Optoelectronics. J. Am. Chem. Soc. 2015, 137, 11038−11046.

(9) Titi, H. M.; Tripuramallu, B. K.; Goldberg, I. Porphyrin-based assemblies directed by non-covalent interactions. Highlights of recent investigations. CrystEngComm 2016, 18, 3183−3339.

(10) Li, B.; Zang, S.-Q.; Wang, L.-Y.; Mak, T. C. W. Halogen bonding: A powerful, emerging tool for constructing high-dimensional metal-containing supramolecular networks. Coord. Chem. Rev. 2016, 308, 1−21.

(11) Mukherjee, A.; Teyssandier, J.; Hennrich, G.; De Feyter, S.; Mali, K. S., Two-dimensional crystal engineering using halogen and hydrogen bonds: towards structural landscapes. Chem. Sci. 2017. 8375910.1039/C7SC00129K

(12) Saha, S.; Desiraju, G. R. Crystal Engineering of Hand-Twisted Helical Crystals. J. Am. Chem. Soc. 2017, 139, 1975−1983.

(13) Lu, Y.; Shi, T.; Wang, Y.; Yang, H.; Yan, X.; Luo, X.; Jiang, H.; Zhu, W. Halogen Bonding−A Novel Interaction for Rational Drug Design? J. Med. Chem. 2009, 52, 2854−2862.

(14) Hardegger, L. A.; Kuhn, B.; Spinnler, B.; Anselm, L.; Ecabert, R.; Stihle, M.; Gsell, B.; Thoma, R.; Diez, J.; Benz, J.; Plancher, J.-M.; Hartmann, G.; Banner, D. W.; Haap, W.; Diederich, F. Systematic Investigation of Halogen Bonding in Protein−Ligand Interactions. Angew. Chem., Int. Ed. 2011, 50, 314−318.

(15) Wilcken, R.; Zimmermann, M. O.; Lange, A.; Joerger, A. C.; Boeckler, F. M. Principles and Applications of Halogen Bonding in Medicinal Chemistry and Chemical Biology. J. Med. Chem. 2013, 56, 1363−1388.

(16) Bruckmann, A.; Pena, M. A.; Bolm, C. Organocatalysis through Halogen-Bond Activation. Synlett 2008, 2008, 900−902.

(17) Kniep, F.; Jungbauer, S. H.; Zhang, Q.; Walter, S. M.; Schindler, S.; Schnapperelle, I.; Herdtweck, E.; Huber, S. M. Organocatalysis by Neutral Multidentate Halogen-Bond Donors. Angew. Chem., Int. Ed. 2013, 52, 7028−7032.

(18) Desiraju, G. R.; Shing Ho, P.; Kloo, L.; Legon, A. C.; Marquardt, R.; Metrangolo, P.; Politzer, P.; Resnati, G.; Rissanen, K. Definition of

DOI: 10.1021/acs.cgd.8b00398
Cryst. Growth Des. 2018, 18, 3244−3254

the halogen bond (IUPAC recommendations 2013). Pure Appl. Chem. 2013, 85, 1711−1713.
(19) Lommerse, J. P. M.; Stone, A. J.; Taylor, R.; Allen, F. H. The Nature and Geometry of Intermolecular Interactions between Halogens and Oxygen or Nitrogen. J. Am. Chem. Soc. 1996, 118, 3108−3116.
(20) Clark, T.; Hennemann, M.; Murray, J. S.; Politzer, P. Halogen bonding: the σ-hole. J. Mol. Model. 2007, 13, 291−296.
(21) Politzer, P.; Murray, J. S.; Clark, T. Halogen bonding and other σ-hole interactions: a perspective. Phys. Chem. Chem. Phys. 2010, 12, 7748−7757.
(22) Metrangolo, P.; Resnati, G. Type II halogen···halogen contacts are halogen bonds. IUCrJ 2014, 1, 5−7.
(23) Metrangolo, P.; Meyer, F.; Pilati, T.; Resnati, G.; Terraneo, G. Halogen Bonding in Supramolecular Chemistry. Angew. Chem., Int. Ed. 2008, 47, 6114−6127.
(24) Cavallo, G.; Metrangolo, P.; Milani, R.; Pilati, T.; Priimagi, A.; Resnati, G.; Terraneo, G. The Halogen Bond. Chem. Rev. 2016, 116, 2478−2601.
(25) Wang, C.; Danovich, D.; Mo, Y.; Shaik, S. On The Nature of the Halogen Bond. J. Chem. Theory Comput. 2014, 10, 3726−3737.
(26) Hathwar, V. R.; Gonnade, R. G.; Munshi, P.; Bhadbhade, M. M.; Guru Row, T. N. Guru Row, T. N., Halogen Bonding in 2,5-Dichloro-1,4-benzoquinone: Insights from Experimental and Theoretical Charge Density Analysis. Cryst. Growth Des. 2011, 11, 1855−1862.
(27) Tsuzuki, S.; Uchimaru, T.; Wakisaka, A.; Ono, T.; Sonoda, T. CCSD(T) level interaction energy for halogen bond between pyridine and substituted iodobenzenes: origin and additivity of substituent effects. Phys. Chem. Chem. Phys. 2013, 15, 6088−6096.
(28) Alkorta, I.; Sanchez-Sanz, G.; Elguero, J. Linear free energy relationships in halogen bonds. CrystEngComm 2013, 15, 3178−3186.
(29) Dumele, O.; Wu, D.; Trapp, N.; Goroff, N.; Diederich, F. Halogen Bonding of (Iodoethynyl)benzene Derivatives in Solution. Org. Lett. 2014, 16, 4722−4725.
(30) Ellington, T. L.; Reves, P. L.; Simms, B. L.; Wilson, J. L.; Watkins, D. L.; Tschumper, G. S.; Hammer, N. I. Quantifying the Effects of Halogen Bonding by Haloaromatic Donors on the Acceptor Pyrimidine. ChemPhysChem 2017, 18, 1267−1273.
(31) Oliveira, V.; Kraka, E.; Cremer, D. Quantitative Assessment of Halogen Bonding Utilizing Vibrational Spectroscopy. Inorg. Chem. 2017, 56, 488−502.
(32) Metrangolo, P.; Resnati, G. Halogen Bonding: A Paradigm in Supramolecular Chemistry. Chem. - Eur. J. 2001, 7, 2511−2519.
(33) De Santis, A.; Forni, A.; Liantonio, R.; Metrangolo, P.; Pilati, T.; Resnati, G. N···Br Halogen Bonding: One-Dimensional Infinite Chains through the Self-Assembly of Dibromotetrafluorobenzenes with Dipyridyl Derivatives. Chem. - Eur. J. 2003, 9, 3974−3983.
(34) Hauchecorne, D.; Szostak, R.; Herrebout, W. A.; van der Veken, B. J. C X···O Halogen Bonding Interactions of Trifluoromethyl Halides with Dimethyl Ether. ChemPhysChem 2009, 10, 2105−2115.
(35) Nagels, N.; Hauchecorne, D.; Herrebout, W. A., Exploring the C-X···π Halogen Bonding Motif: An Infrared and Raman Study of the Complexes of CF3X (X = Cl, Br and I) with the Aromatic Model Compounds Benzene and Toluene. Molecules 2013, 18, 6829−10. 3390/molecules18066829
(36) Aakeröy, C. B.; Wijethunga, T. K.; Desper, J.; Đaković, M. Crystal Engineering with Iodoethynylnitrobenzenes: A Group of Highly Effective Halogen-Bond Donors. Cryst. Growth Des. 2015, 15, 3853−3861.
(37) Cerreia Vioglio, P.; Catalano, L.; Vasylyeva, V.; Nervi, C.; Chierotti, M. R.; Resnati, G.; Gobetto, R.; Metrangolo, P. Natural Abundance 15N and 13C Solid-State NMR Chemical Shifts as High Sensitivity Probes of the Halogen Bond Geometry. Chem. - Eur. J. 2016, 22, 16819−16828.
(38) Messina, M. T.; Metrangolo, P.; Navarrini, W.; Radice, S.; Resnati, G.; Zerbi, G. Infrared and Raman analyses of halogen-bonded non-covalent adducts formed by α,ω-diiodoperfluoroalkanes with DABCO and other electron donors. Mol. Struct. 2000, 524, 87−94.
(39) Hawthorne, B.; Fan-Hagenstein, H.; Wood, E.; Smith, J.; Hanks T. Study of the Halogen Bonding between Pyridine and Perfluoroalk Iodide in Solution Phase Using the Combination of FTIR and 19F NMR. Int. J. Spectrosc. 2013, 2013, 1−10.
(40) Nagels, N.; Herrebout, W. A. A cryospectroscopic infrared and Raman study of the CX···π halogen bonding motif: Complexes of th CF3Cl, CF3Br, and CF3I with ethyne, propyne, and 2-butyne. Spectrochim. Acta, Part A 2015, 136, 16−26.
(41) Vasylyeva, V.; Catalano, L.; Nervi, C.; Gobetto, R.; Metrangolo, P.; Resnati, G. Characteristic red shift and intensity enhancement of far-IR fingerprints of the halogen bond involving aromatic donors. CrystEngComm 2014, 16, 2247−2250.
(42) Politzer, P.; Murray, J. S. In Noncovalent Forces; Scheiner, S., I Springer International Publishing: Cham, 2015; pp 291−321.
(43) Nguyen, S. T.; Rheingold, A. L.; Tschumper, G. S.; Watkins, D. L. Elucidating the Effects of Fluoro and Nitro Substituents on Halog Bond Driven Assemblies of Pyridyl-Capped π-Conjugated Molecules. Cryst. Growth Des. 2016, 16, 6648−6653.
(44) Pang, X.; Jin, W. J. Exploring the halogen bond specific solvent effects in halogenated solvent systems by ESR probes. New J. Chem. 2015, 39, 5477−5483.
(45) Hauchecorne, D.; Herrebout, W. A. Experimental Characterization of C−X···Y−C (X = Br, I; Y = F, Cl) Halogen−Halogen Bonds. J. Phys. Chem. A 2013, 117, 11548−11557.
(46) Franklin-Mergarejo, R.; Rubayo-Soneira, J.; Halberstadt, N.; Janda, K. C.; Apkarian, V. A. A theoretical simulation of the resonant Raman spectroscopy of the H2O···Cl2 and H2O···Br2 halogen-bonded complexes. J. Chem. Phys. 2016, 144, 054307.
(47) Bosch, E. Serendipity and the Search for Short N−I Halogen Bonds. Cryst. Growth Des. 2014, 14, 126−130.
(48) Dolomanov, O. V.; Bourhis, L. J.; Gildea, R. J.; Howard, J. A. K.; Puschmann, H. OLEX2: a complete structure solution, refinement and analysis program. J. Appl. Crystallogr. 2009, 42, 339−341.
(49) Foster, J. P.; Weinhold, F. Natural hybrid orbitals. J. Am. Chem. Soc. 1980, 102, 7211−7218.
(50) Reed, A. E.; Weinhold, F. Natural bond orbital analysis of near-Hartree-Fock water dimer. J. Chem. Phys. 1983, 78, 4066−4073.
(51) Reed, A. E.; Weinhold, F. Natural localized molecular orbitals. J. Chem. Phys. 1985, 83, 1736−1740.
(52) Reed, A. E.; Weinstock, R. B.; Weinhold, F. Natural population analysis. J. Chem. Phys. 1985, 83, 735−746.
(53) Reed, A. E.; Curtiss, L. A.; Weinhold, F. Intermolecular interactions from a natural bond orbital, donor-acceptor viewpoint. Chem. Rev. 1988, 88, 899−926.
(54) Carpenter, J. E.; Weinhold, F. Analysis of the geometry of the hydroxymethyl radical by the "different hybrids for different spins" natural bond orbital procedure. J. Mol. Struct.: THEOCHEM 1988, 169, 41−62.
(55) Wiberg, K. B.; Bader, R. F. W.; Lau, C. D. H. Theoretical analysis of hydrocarbon properties. 1. Bonds, structures, charge concentrations, and charge relaxations. J. Am. Chem. Soc. 1987, 109, 985−1001.
(56) The Structure of Small Molecules and Ions; Springer US: 1988.
(57) Boys, S. F.; Bernardi, F. The calculation of small molecular interactions by the differences of separate total energies. Some procedures with reduced errors. Mol. Phys. 1970, 19, 553−566.
(58) Simon, S.; Duran, M.; Dannenberg, J. J. How does basis set superposition error change the potential surfaces for hydrogen-bon dimers? J. Chem. Phys. 1996, 105, 11024−11031.
(59) Dunning, T. H. Gaussian basis sets for use in correlated molecular calculations. I. The atoms boron through neon and hydrogen. J. Chem. Phys. 1989, 90, 1007−1023.
(60) Kendall, R. A.; Dunning, T. H.; Harrison, R. J. Electron affinities of the first-row atoms revisited. Systematic basis sets and wave functions. J. Chem. Phys. 1992, 96, 6796−6806.
(61) Frisch, M. J.; Trucks, G. W.; Schlegel, H. B.; Scuseria, G. E.; Robb, M. A.; Cheeseman, J. R.; Scalmani, G.; Barone, V.; Mennucci, B.; Petersson, G. A.; Nakatsuji, H.; Caricato, M.; Li, X.; Hratchian, H. P.; Izmaylov, A. F.; Bloino, J.; Zheng, G.; Sonnenberg, J. L.; Hada, M.;

DOI: 10.1021/acs.cgd.8b00398
Cryst. Growth Des. 2018, 18, 3244−3254

Ehara, M.; Toyota, K.; Fukuda, R.; Hasegawa, J.; Ishida, M.; Nakajima, T.; Honda, Y.; Kitao, O.; Nakai, H.; Vreven, T.; Montgomery, J. A., Jr.; Peralta, J. E.; Ogliaro, F.; Bearpark, M. J.; Heyd, J.; Brothers, E. N.; Kudin, K. N.; Staroverov, V. N.; Kobayashi, R.; Normand, J.; Raghavachari, K.; Rendell, A. P.; Burant, J. C.; Iyengar, S. S.; Tomasi, J.; Cossi, M.; Rega, N.; Millam, N. J.; Klene, M.; Knox, J. E.; Cross, J. B.; Bakken, V.; Adamo, C.; Jaramillo, J.; Gomperts, R.; Stratmann, R. E.; Yazyev, O.; Austin, A. J.; Cammi, R.; Pomelli, C.; Ochterski, J. W.; Martin, R. L.; Morokuma, K.; Zakrzewski, M. G.; Voth, G. A.; Salvador, P.; Dannenberg, J. J.; Dapprich, S.; Daniels, A. D.; Farkas, Ö.; Foresman, J. B.; Ortiz, J. V.; Cioslowski, J.; Fox, D. J. Gaussian, Inc.: Wallingford, CT, USA, 2009.
(62) Zhao, Y.; Truhlar, D. G. The M06 suite of density functionals for main group thermochemistry, thermochemical kinetics, noncovalent interactions, excited states, and transition elements: two new functionals and systematic testing of four M06-class functionals and 12 other functionals. Theor. Chem. Acc. 2008, 120, 215−241.
(63) Peterson, K. A.; Shepler, B. C.; Figgen, D.; Stoll, H. On the Spectroscopic and Thermochemical Properties of ClO, BrO, IO, and Their Anions. J. Phys. Chem. A 2006, 110, 13877−13883.
(64) Kozuch, S.; Martin, J. M. L. Halogen Bonds: Benchmarks and Theoretical Analysis. J. Chem. Theory Comput. 2013, 9, 1918−1931.
(65) Lu, T.; Chen, F. Multiwfn: A multifunctional wavefunction analyzer. J. Comput. Chem. 2012, 33, 580−592.
(66) Herrebout, W. In Halogen Bonding I: Impact on Materials Chemistry and Life Sciences; Metrangolo, P., Resnati, G., Eds.; Springer International Publishing: Cham, 2015; p 79−154.
(67) Mei, J.; Diao, Y.; Appleton, A. L.; Fang, L.; Bao, Z. Integrated Materials Design of Organic Semiconductors for Field-Effect Transistors. J. Am. Chem. Soc. 2013, 135, 6724−6746.
(68) Hendsbee, A. D.; Sun, J.-P.; McCormick, T. M.; Hill, I. G.; Welch, G. C. Unusual loss of electron mobility upon furan for thiophene substitution in a molecular semiconductor. Org. Electron. 2015, 18, 118−125.
(69) Sonar, P.; Chang, J.; Shi, Z.; Wu, J.; Li, J. Thiophene-tetrafluorophenyl-thiophene: a promising building block for ambipolar organic field effect transistors. J. Mater. Chem. C 2015, 3, 2080−2085.
(70) Tsuji, H.; Nakamura, E. Design and Functions of Semiconducting Fused Polycyclic Furans for Optoelectronic Applications. Acc. Chem. Res. 2017, 50, 396−406.
(71) Takimiya, K.; Osaka, I.; Mori, T.; Nakano, M. Organic Semiconductors Based on [1]Benzothieno[3,2-b][1]benzothiophene Substructure. Acc. Chem. Res. 2014, 47, 1493−1502.
(72) Goud, N. R.; Bolton, O.; Burgess, E. C.; Matzger, A. J. Unprecedented Size of σ-Holes on 1,3,5-Triiodo-2,4,6-trinitrobenzene Begets Unprecedented Intermolecular Interactions. Cryst. Growth Des. 2016, 16, 1765−1771.
(73) Politzer, P.; Murray, S. J. σ-Hole Interactions: Perspectives and Misconceptions. Crystals 2017, 7,
(74) Clark, T. Halogen bonds and [sigma]-holes. Faraday Discuss. 2017. 203 9 10.1039/C7FD00058H
(75) Rahm, M.; Hoffmann, R.; Ashcroft, N. W. Atomic and Ionic Radii of Elements 1−96. Chem. - Eur. J. 2016, 22, 14625−14632.
(76) Aakeröy, C. B.; Baldrighi, M.; Desper, J.; Metrangolo, P.; Resnati, G. Supramolecular Hierarchy among Halogen-Bond Donors. Chem. - Eur. J. 2013, 19, 16240−16247.
(77) Fox, D. B.; Liantonio, R.; Metrangolo, P.; Pilati, T.; Resnati, G. Perfluorocarbon-hydrocarbon self-assembly, halogen bonding mediated intermolecular recognition. J. Fluorine Chem. 2004, 125, 271−281.
(78) Wang, C.; Danovich, D.; Shaik, S.; Mo, Y. A Unified Theory for the Blue and Red-Shifting Phenomena in Hydrogen and Halogen Bonds. J. Chem. Theory Comput. 2017, 13, 1626−1637.
(79) Wang, P.; Zhao, N.; Tang, Y. Halogen Bonding in the Complexes of CH_3I and CCl_4 with Oxygen-Containing Halogen-Bond Acceptors. J. Phys. Chem. A 2017, 121, 5045−5055.
(80) Merz, K. M. Secondary interactions in 1-iodo-3-nitrobenzene and 1-iodo-3,5-dinitrobenzene. Acta Crystallogr., Sect. C: Cryst. Struct. Commun. 2003, 59, o65−o67.

DOI: 10.1021/acs.cgd.8b00398
Cryst. Growth Des. 2018, 18, 3244−3254